Title

Scaling of the strange-metal scattering in unconventional superconductors

Journal

Nature, 602(7897)

ISSN

0028-0836

Authors

Yuan, Jie

Chen, Qihong

Jiang, Kun

et al.

Publication Date

2022-02-17

DOI

10.1038/s41586-021-04305-5

Peer reviewed

Scaling of the strange-metal scattering in unconventional superconductors

Jie Yuan[1,2,7], Qihong Chen[1,3,7], Kun Jiang[1], Zhongpei Feng[1,3], Zefeng Lin[1], Heshan Yu[1], Ge He[1], Jinsong Zhang[1], Xingyu Jiang[1], Xu Zhang[1], Yujun Shi[1], Zhi Gang Cheng[1,3], Nobumichi Tamura[4], Yifeng Yang[1], Jiangping Hu[1,3], Ichiro Takeuchi[5,6], Kui Jin[1,3], and Zhongxian Zhao[1,3]

[1]Beijing National Laboratory for Condensed Matter Physics, Institute of Physics, Chinese Academy of Sciences, Beijing 100190, China.

[2]Key Laboratory of Vacuum Physics, School of Physical Sciences, University of Chinese Academy of Sciences, Beijing 100049, China

[3]Songshan Lake Materials Laboratory, Dongguan, Guangdong 523808, China.

[4]Advanced Light Source, Lawrence Berkeley National Laboratory, Berkeley, CA 94720, USA

[5]Department of Materials Science and Engineering, University of Maryland, College Park, MD 20742, USA.

[6]Quantum Materials Center, University of Maryland, College Park, MD 20742, USA.

[7]These authors contributed equally.

Abstract: Dramatic evolution of properties with minute change in the doping level is a hallmark of the complex chemistry which governs cuprate superconductivity as manifested in the celebrated superconducting domes as well as quantum criticality taking place at precise compositions[1–4]. The linear-in-temperature resistivity has emerged as a central feature in the normal state of cuprate superconductors[5–9]. The ubiquity of this strange metal behavior seems to signal an intimate link between the scattering mechanism and superconductivity[10–12], and yet a clear picture of the correlation between the doping level, scattering rate, and occurrence of superconductivity has been lacking. Here, we report the observation of quantitative scaling laws of the superconducting transition temperature T_c and the scattering rate of the linear-in-temperature resistivity as a precise function of the doping level in electron-doped cuprate $La_{2-x}Ce_xCuO_4$ (LCCO). High-resolution characterization of epitaxial composition-spread thin films has allowed us to systematically map the structural and transport properties of LCCO with unprecedented accuracy and increment of $\Delta x = 0.0015$. We uncover the relations $T_c \sim (x_c\text{-}x)^{0.5} \sim (A_1^{\square})^{0.5}$, where x_c is the critical doping where superconductivity disappears at the overdoped

side, and $A_1^{\square}$ is the scattering rate of perfect *T*-linear resistivity per CuO_2 plane. There is a striking universality of the T_c vs $A_1^{\square}$ relation among cuprates, iron-based and organic superconductors which may be pointing to a common mechanism for these unconventional superconductors.

Main text:

The strange metallic behavior in the normal-state resistivity of cuprate superconductors was first observed shortly after their discovery. The unusual behavior where the resistivity varies as a linear function of temperature (linear-in-*T* resistivity) has now been reported in a number of superconducting copper oxides up to several hundred kelvin[5,6]. In a narrow composition region around optimal doping, the linear-in-*T* behavior extends to low temperatures (close to T_c)[6], indicating a critical behavior at the quantum critical point (QCP). In a hole-doped copper oxide $La_{2-x}Sr_xCuO_4$ (LSCO), the linear-in-*T* resistivity component was found to dominate the normal-state transport properties down to 1.5 K in pulsed high magnetic fields, within an extended range near the optimal doping[7]. For electron-doped copper oxides, a perfect linear-in-*T* resistivity was found to persist down to 40 mK in $Pr_{2-x}Ce_xCuO_4$[8] and to 20 mK in $La_{2-x}Ce_xCuO_4$ (LCCO)[9]. In particular, this strange metal behavior in LCCO was found to persist from the doping level associated with the Fermi surface reconstruction ($x \approx 0.14$) to the end point of the superconducting dome. Moreover, the scattering rate of linear-in-*T* resistivity (i.e., the coefficient A_1 from $\rho = \rho_0 + A_1T$) shows a positive correlation with T_c, pointing to a common origin shared by the anomalous normal state and the superconductivity[9,10].

To this end, there has been a concerted effort in the community to quantify the relationship between A_1 and T_c as a direct function of the chemical doping concentration[10,11]. However, due to the lack of sufficient data points with enough density to map across the doping phase diagrams, an explicit expression had been elusive. Here, we have employed high-precision thin-film composition spreads encompassing the entire concentration range of the electron-doped superconducting

dome with incremental accuracy in doping concentration Δx of 0.0015. The systematic measurements have uncovered a remarkable scaling law linking the superconducting transition temperature (T_c), doping level (x) and the T-linear coefficient ($A_1^{\square}$), namely $T_c \sim (x_c\text{-}x)^{0.5} \sim (A_1^{\square})^{0.5}$, which is observed here for the first time. Our finding then points to a striking universal relation between the normalized T-linear coefficient and T_c among cuprates, pnictides, and a class of organic superconductors, strongly suggestive of a common underlying physics at work in these unconventional superconductors.

For the family of electron-doped copper oxide superconductor LCCO, the superconducting phase is the so-called T' phase, which is only stable in the form of thin films. Upon doping, LCCO evolves from a weakened antiferromagnetic (AF) state to a superconducting phase with a dome-shaped phase diagram[3]. At the endpoint of the superconducting region ($x_c \approx 0.175 \pm 0.005$), it enters a metallic (non-superconducting) Fermi liquid state[11], and in the vicinity of this QCP ($0.14 < x < 0.17$), a strange metal state appears in the low-temperature limit (down to 20 mK) upon suppressing the superconductivity with magnetic fields[9]. Very recently, the strange metal state has also been observed in the antiferromagnetic regime (e.g. x = 0.12, 0.13)[13].

This calls for comprehensive mapping of the subtle concentration-dependent properties across this narrow composition range, and yet because of the relatively complex synthesis process, it is nontrivial to tune the composition of LCCO films with high precision. We upend this challenge by enlisting the composition spread synthesis combined with micron-scale systematic characterization. Employing combinatorial laser molecular beam epitaxy[14,15], we have fabricated continuous composition spread LCCO films possessing a linear gradient in the Ce content along a predesigned sample direction with demonstrated composition variation accuracy of Δx = 0.0015 across the superconducting dome.

The synthesis scheme is shown in Fig. 1a. Two targets with nominal compositions of $La_{1.90}Ce_{0.10}CuO_4$ and $La_{1.81}Ce_{0.19}CuO_4$ are used as two ends of the composition spreads, corresponding to the optimal doping (x = 0.10) with highest T_c

and the metallic Fermi liquid state (x = 0.19), respectively. A series of unitcell-thick gradient wedges are deposited with the two targets in an alternating manner using moving mechanical shutters at 700 °C on a $SrTiO_3$ (STO) (100) substrate which results in a c-axis oriented epitaxial composition spread LCCO thin film with continuously varying composition and uniform total thickness across the 10 mm length of the substrate. This growth technique ensures that the synthesis conditions are identical for the entire doping range.

We first perform standard "low resolution" analysis of composition and the corresponding c-axis lattice constant variation across the spread using wavelength-dispersive x-ray spectroscopy (WDS) and an in-house diffractometer, respectively. As shown in the lower panel of Fig. 1a, the WDS-mapped Ce concentration in the LCCO film shows the expected dependence on position, spanning $0.10 \leq x \leq 0.19$, as designed. The uncertainty in determined concentration from WDS is typically 2%. Figure 1b shows the $\theta/2\theta$ x-ray diffraction (XRD) patterns scanning across the film along the direction of compositional gradient. The lower panel of Fig. 1b shows the LCCO (006) (left) and STO (002) (right) Bragg peaks mapped along the spread. The LCCO (006) peak clearly moves to higher angles as the doping concentration is increased, whereas the STO (002) peak does not change. Figure 1c shows the lattice constant mapping across the spread chip with error bars determined by limitations of an in-house diffractometer operated under standard conditions with the beam size of 0.4 mm. Despite the smooth and well-behaved overall variations of the composition and the lattice constant over the entire length of the spread, the measurement uncertainties set the resolution limits for carrying out systematic composition-dependent physical property characterization.

In order to harness the wealth of information which resides in the epitaxial spread at high spatial resolution, we enlist synchrotron microbeam diffraction whose beam spot size of 1 micron (together with micron-level accuracy of its scanning stage) allows the ultimate determination of the composition variation sensitivity and the smallest meaningful increment with which we can extract composition-dependent properties from the spread. Figure 1d shows the lattice constant mapping obtained

from a part of the spread using the microbeam with 20 micron position increment across the spread (taken at BL-XX at ALS). The variation of the lattice constant from point to point as well as its linear regression indicates that it can be determined with the uncertainty of 0.001 Å, which corresponds to the compositional variation Δx of 0.0015. We note that such accuracy in composition control is not possible with traditional chemical synthesis methods[9]. Since positions on the spread can be readily specified with accuracy down to microns, these numbers indicate we can obtain statistically significant mapping of composition-dependent properties with high incremental density within the 10 mm length of the spread encompassing $\Delta x \approx 0.09$.

The transport properties are obtained by patterning the spread film into micro-bridge arrays, as schematically shown in Fig. 2a. Initially, the LCCO spread film is patterned into 8 bridges, each with a width of 0.9 mm, for rapidly surveying the superconducting properties over the entire spread. Each bridge is then divided into 8 smaller bridges, each with a width of 100 μm. At the last step, some bridges with compositions near where the superconductivity disappears can be further patterned into 20 μm wide bridges in order to study the delicate critical behavior.

The $R(T)$ data obtained from all 100-micron bridges across the entire spread are shown in Fig. 2b. Near the lower x end (≈ 0.11), LCCO shows superconductivity with the highest $T_c \approx 24$ K (the bottom curve). Here, T_c is defined as the temperature where the superconducting transition commences, as illustrated in Supplementary Fig. S3. With increasing doping level, T_c gradually decreases, and eventually bridges with higher Ce content only show metallic behavior, i.e. the resistivity decreases with decreasing temperature but no abrupt drop of resistance is seen even at the lowest measured temperature of 2 K. The critical composition at which the superconductivity disappears corresponds to the doping level of $x_c = 0.177$, consistent with previous results[9,16]. For $x > x_c$, the low-temperature dependence of resistivity obeys the Fermi liquid behavior, namely $\rho = \rho_0 + A_2T^2$ (Fig. 2c), and the T^2 dependence persists to higher temperatures with increasing Ce content[9]. For $x < x_c$, the normal-state resistivity shows linear-in-T behavior at low temperatures, which is ubiquitous in copper oxide superconductors. With the superconductivity suppressed by magnetic fields (applied

perpendicular to the film), the linear-in-T region extends down to the lowest measured temperature, where the experimental data can be fitted well by $\rho = \rho_0 + A_1 T$ (Fig. 2d).

The top panel of Fig. 3a shows the doping dependence of T_c^{on} for two LCCO composition spread films. As seen in Fig. 3a, compared with the limited data points from samples made by the traditional synthesis method (blue squares, adapted from Ref [9]), a clear trend emerges in the dense data from the present combinatorial technique: the red line, which outlines the boundary of the superconducting phase obeys the square root relation $T_c \propto (x_c - x)^{\frac{1}{2}}$. The square root dependence has previously been used to fit the data of the hole-doped superconductor LSCO in the overdoped region[17]. Here, we are able to clearly discern it for the electron-doped LCCO in the overdoped superconducting regime for the first time.

Now we turn to the strange metal state in LCCO. We have extracted the T-linear coefficient A_1 from all 100-micron bridge curves shown here in the bottom panel of Fig. 3a as a function of the continuous doping level. As introduced by A. Legros *et al.*[18], we normalize A_1 by the distance between adjacent CuO_2 planes, i.e. $A_1^{\square} = A_1/d$, where d is half of the c-axis lattice constant mapped accurately across the spread. An unmistakable linear dependence of $A_1^{\square}$ on doping (x) emerges as a result. We note that prior to this work, the relation between A_1 and the doping level had not been unambiguously quantified due to serious scattering of data points[10,19]. Without the combinatorial approach, it is difficult to obtain such accurate and systematic data. The newly unearthed relations in turn then immediately point to the square root dependence of T_c on $A_1^{\square}$: Fig. 3b shows T_c vs $(A_1^{\square})^{0.5}$ with the red line given by the linear fit $(A_1^{\square})^{0.5} = \alpha T_c + \beta$, with $\alpha = 0.10\ (\Omega K^{-1})^{0.5}/K$ and $\beta = 1.22\ (\Omega K^{-1})^{0.5}$. Hence, a linear relation between $(A_1^{\square})^{0.5}$ and T_c is established in LCCO.

This relation allows us to make quantitative comparisons with other unconventional superconductor systems. For the typical hole-doped copper oxide LSCO, the $A_1^{\square}(T_c)$ relation is extracted from a comprehensive study by Bozovic *et al.* [20]. As shown in Fig. 3c, the $A_1^{\square}$ shows a similar dependence on T_c. Beyond cuprates, the relation between $A_1^{\square}$ and T_c has also been observed in the single-band organic

superconductor $(TMTSF)_2PF_6$ as well as in the iron-based superconductor $Ba(Fe_{1-x}Co_x)_2As_2$. As seen in Fig. 3c, there is a single scaling relation which captures the shared behavior among the disparate unconventional superconductors, suggestive of a universal underlying excitation governing their pairing mechanism.

This universal scaling relation places an explicit constraint on the general theory of linear-in-T resistivity and unconventional superconductivity. Various theoretical descriptions[4,12,21–24] have been proposed to explain the linear-in-T resistivity in copper oxides to date. One scenario attracting much attention involves the Planckian dissipation[18,24], where the scattering rate reaches the fundamental Planckian limit given by $\hbar/\tau = k_B T$. It can be used to explain the linear-in-T resistivity in hole-doped copper oxides from high temperatures to the lowest measured temperature of 2 K. From $\Delta\rho = \rho - \rho_0 = m^*/ne^2\tau$ and the Planckian dissipation $\hbar/\tau = k_B T$, we obtain $\Delta\rho = \frac{m^* k_B}{ne^2\hbar}T$. Previous studies have shown that in high-T_c cuprates, the superfluid phase stiffness goes as $\rho_s \propto T_c$ and the superfluid density varies as $n_s \propto n$[20,25]. These relations lead to $A_1^{\square} \propto m^*/n \; m^*/n_s \; (\rho_s)^{-1} \; (T_c)^{-1}$, which is clearly in disagreement with the present observation of the positive correlation between $A_1^{\square}$ and T_c. This puzzle needs to be resolved before this scenario can be applied to the overdoped side of copper oxides.

Another plausible origin of the linear-in-T resistivity is the AF spin fluctuations associated with quantum criticality[3,23,26]. This picture is best substantiated in $(TMTSF)_2PF_6$, where superconductivity arises from a spin density wave (SDW) order and a perfect linear-in-T resistivity is observed as T approaches zero[10,27,28]. With the absence of a pseudogap phenomenon and other anomalous electronic phases in $(TMTSF)_2PF_6$, it is widely accepted that its behaviors are intimately tied to short-range SDW fluctuations[3,10], which is the dominant source for transport scattering at low temperatures[29]. Given the very similar transport properties and evolution of ground

states in the phase diagrams between electron-doped LCCO and $(TMTSF)_2PF_6$, the linear-in-T scattering and superconductivity in electron-doped copper oxides are perhaps also governed by AF spin fluctuations[9,11]. Analogous behaviors are also found in the iron-based superconductor $Ba(Fe_{1-x}Co_x)_2As_2$[30]. Although the picture is more complex in hole-doped copper oxides involving a complex pseudogap and intertwined orders[31], the single scaling relation observed here might be the common signature of interplay among linear-in-T resistivity, pairing correlations and spin fluctuations[10,29]. A microscopic description of how the pairing is mediated by spin fluctuations remains an open question, but given the universal behavior observed across different families of superconductors, renewed and focused theoretical investigations are perhaps in order.

It should be noted that in Fig. 3b the linear fitting of $(A_1^{\square})^{0.5}$ extrapolates to a finite value at $T_c = 0$. However, approaching the QCP at the end of the superconducting dome where $T_c = 0$, the linear-in-T resistivity disappears, i.e. A_1 becomes zero[9]. This discrepancy is possibly due to quantum fluctuations or strong pairing fluctuations[32] close to QCP, and thus $(A_1^{\square})^{0.5}$ deviates from the linear dependence. Unfortunately, due to the uncertainties in T_c determination and the reduced temperature range for linear resistivity close to QCP, the error bars of $A_1^{\square}$ and T_c become large thus a quantitative description is difficult to achieve. Further investigations are required to clarify this issue, which may provide further insight into the origin of superconductivity in the overdoped side of LCCO.

Acknowledgements

We are greatly indepted to Richard Greene for many fruitful discussions and inspiring comments during the preparation of the manuscript. We would like to thank Tao Xiang and Yuan Li for fruitful discussions. This work was supported by the National Key Basic Research Program of China (2017YFA0302902, 2016YFA0300301, 2017YFA0303003 and 2018YFB0704102), the National Natural Science Foundation of China (11927808 11834016 118115301 and 119611410, 11961141008), the Strategic Priority Research Program (B) of Chinese Academy of Sciences (XDB25000000, XDB33000000), the Key Research Program of Frontier Sciences, CAS (QYZDB-SSW-SLH008 and QYZDY-SSW-SLH001), CAS Interdisciplinary Innovation Team, Beijing Natural Science Foundation (Z190008), Key-Area Research

and Development Program of Guangdong Province(2020B0101340002).

Author Contributions

K.J. and J.Y. conceived the project. K.J., J.Y. and Q.H.C supervised the experiments. H.S.Y., Z.P.F and Z.F.L. synthesized high-throughput LCCO films. Z.F.L., G.H. and X.Z. performed the transport measurements. N.T. and I.T. did the synchrotron XRD measurements. J.Y., Q.H.C, I.T. and K.J. analyzed the data and wrote the manuscript with input from all authors.

Methods

Film growth. We fabricate combinatorial $La_{2-x}Ce_xCuO_{4\pm\delta}$ (x = 0.10 ~ 0.19) thin films on one $SrTiO_3$ (STO) substrate (10×10 mm^2 in size) with programmed-motion mask. The targets *A* and *B* are $La_{1.9}Ce_{0.1}CuO_{4\pm\delta}$ (i.e., x = 0.10) and $La_{0.81}Ce_{0.19}CuO_{4\pm\delta}$ (i.e., x = 0.19), respectively. When the targets were ablated alternately by ultraviolet KrF laser pulses (λ = 248 nm), a moving mask with constant speed was used to achieve opposite linear abundance ratio distribution of two precursors. The deposition ratio was carefully controlled to ensure that the film deposited in one period never exceeded a single-cell layer to avoid the appearance of superlattices. After eighty periods, a 100 nm thick combinatorial $La_{2-x}Ce_xCuO_{4\pm\delta}$ (LCCO) film is achieved after the *in situ* reduction process of several minutes in vacuum at about 700 °C.

Structural characterization. The crystalline of the whole film is tested by an x-ray diffract meter with micro area measurement unit. The beam size is 0.4 mm in width and set to scan the film from one end to the other. In every step, the 2θ is taken from 10^o to 80^o to achieve the structure of the section with finite doping in the combi-film. The lattice structure of the combi-film is also examined by an advanced synchrotron light source in order to study the lattice evolution with spatial resolution of 1×1 μm^2. Along the doping gradient direction (horizontal) and the same doping direction (vertical), the sampling intervals are 10 μm and 20 μm respectively.

Transport Measurements. The combinatorial thin films were patterned into small chips, to take electrical resistivity from 300 K to low temperature. There are three levels of pattern array with different microbridge width. In this way, the spatial resolution of the transport measurement can reach the scale of 10 μm, comparable to the micro-region structural characterization.

References

1. Lee, P. A., Nagaosa, N. & Wen, X.-G. Doping a Mott insulator: Physics of high-temperature superconductivity. *Rev. Mod. Phys.* **78**, 17–85 (2006).
2. Armitage, N. P., Fournier, P. & Greene, R. L. Progress and perspectives on electron-doped cuprates. *Rev. Mod. Phys.* **82**, 2421–2487 (2010).
3. Scalapino, D. J. A common thread: The pairing interaction for unconventional superconductors. *Rev. Mod. Phys.* **84**, 1383–1417 (2012).
4. Keimer, B., Kivelson, S. A., Norman, M. R., Uchida, S. & Zaanen, J. From quantum matter to high-temperature superconductivity in copper oxides. *Nature* **518**, 179–186 (2015).
5. Gurvitch, M. & Fiory, A. T. Resistivity of $La_{1.825}Sr_{0.175}0.175CuO_4$ and $YBa_2Cu_3O_7$ to 1100 K: Absence of saturation and its implications. *Phys. Rev. Lett.* **59**, 1337–1340 (1987).
6. Takagi, H. *et al.* Systematic evolution of temperature-dependent resistivity in $La_{2-x}Sr_xCuO_4$. *Phys. Rev. Lett.* **69**, 2975–2978 (1992).
7. Cooper, R. A. *et al.* Anomalous Criticality in the Electrical Resistivity of $La_{2-x}Sr_xCuO_4$. *Science* **323**, 603–607 (2009).
8. Fournier, P. *et al.* Insulator-Metal Crossover near Optimal Doping in $Pr_{2-x}Ce_xCuO_4$: Anomalous Normal-State Low Temperature Resistivity. *Phys. Rev. Lett.* **81**, 4720–4723 (1998).
9. Jin, K., Butch, N. P., Kirshenbaum, K., Paglione, J. & Greene, R. L. Link between spin fluctuations and electron pairing in copper oxide superconductors. *Nature* **476**, 73–75 (2011).
10. Taillefer, L. Scattering and Pairing in Cuprate Superconductors. *Annu. Rev. Condens. Matter Phys.* **1**, 51–70 (2010).
11. Greene, R. L., Mandal, P. R., Poniatowski, N. R. & Sarkar, T. The Strange Metal State of the Electron-Doped Cuprates. *Annu. Rev. Condens. Matter Phys.* **11**, 213–229 (2020).
12. Varma, C. M. Colloquium: Linear in temperature resistivity and associated mysteries including high temperature superconductivity. *Rev. Mod. Phys.* **92**, 031001 (2020).
13. Sarkar, T. *et al.* Strange Metallic Transport in the Antiferromagnetic Regime of Electron Doped Cuprates. *ArXiv200712765 Cond-Mat* (2020).
14. Koinuma, H. & Takeuchi, I. Combinatorial solid-state chemistry of inorganic materials. *Nat. Mater.* **3**, 429–438 (2004).
15. Yuan, J., Stanev, V., Gao, C., Takeuchi, I. & Jin, K. Recent advances in high-throughput superconductivity research. *Supercond. Sci. Technol.* **32**, 123001 (2019).
16. Sarkar, T. *et al.* Ferromagnetic order beyond the superconducting dome in a cuprate superconductor. *Science* **368**, 532–534 (2020).
17. Schneider, T. & Singer, J. M. *Phase Transition Approach to High Temperature Superconductivity*. (Imperial College Press, London, 2000). doi:10.1142/p206.
18. Legros, A. *et al.* Universal T-linear resistivity and Planckian dissipation in overdoped cuprates. *Nat. Phys.* **15**, 142–147 (2019).
19. Ayres, J. *et al.* Incoherent transport across the strange metal regime of highly overdoped cuprates. *ArXiv201201208 Cond-Mat* (2020).

20. Božović, I., He, X., Wu, J. & Bollinger, A. T. Dependence of the critical temperature in overdoped copper oxides on superfluid density. *Nature* **536**, 309–311 (2016).
21. Anderson, P. W. The Resonating Valence Bond State in La_2CuO_4 and Superconductivity. *Sci. New Ser.* **235**, 1196–1198 (1987).
22. Varma, C. M., Littlewood, P. B., Schmitt-Rink, S., Abrahams, E. & Ruckenstein, A. E. Phenomenology of the normal state of Cu-O high-temperature superconductors. *Phys. Rev. Lett.* **63**, 1996–1999 (1989).
23. Sachdev, S. Quantum phase transitions. *Phys. World* **12**, 33–38 (1999).
24. Zaanen, J. Why the temperature is high. *Nature* **430**, 512–513 (2004).
25. Tanner, D. B. *et al.* Superfluid and normal fluid density in high-T_c superconductors. *Phys. B Condens. Matter* **244**, 1–8 (1998).
26. Moriya, T. & Ueda, K. Spin fluctuations and high temperature superconductivity. *Adv. Phys.* **49**, 555–606 (2000).
27. Bourbonnais, C. & Sedeki, A. Link between antiferromagnetism and superconductivity probed by nuclear spin relaxation in organic conductors. *Phys. Rev. B* **80**, 085105 (2009).
28. Doiron-Leyraud, N. *et al.* Correlation between linear resistivity and T_c in the Bechgaard salts and the pnictide superconductor $Ba(Fe_{1-x}Co_x)_2As_2$. *Phys. Rev. B* **80**, 214531 (2009).
29. Sedeki, A., Bergeron, D. & Bourbonnais, C. Extended quantum criticality of low-dimensional superconductors near a spin-density-wave instability. *Phys. Rev. B* **85**, 165129 (2012).
30. Fang, L. *et al.* Roles of multiband effects and electron-hole asymmetry in the superconductivity and normal-state properties of $Ba(Fe_{1-x}Co_x)_2As_2$. *Phys. Rev. B* **80**, 140508 (2009).
31. Fradkin, E., Kivelson, S. A. & Tranquada, J. M. Colloquium: Theory of intertwined orders in high temperature superconductors. *Rev. Mod. Phys.* **87**, 457–482 (2015).
32. Maier, T. A., Karakuzu, S. & Scalapino, D. J. Overdoped end of the cuprate phase diagram. *Phys. Rev. Res.* **2**, 033132 (2020).

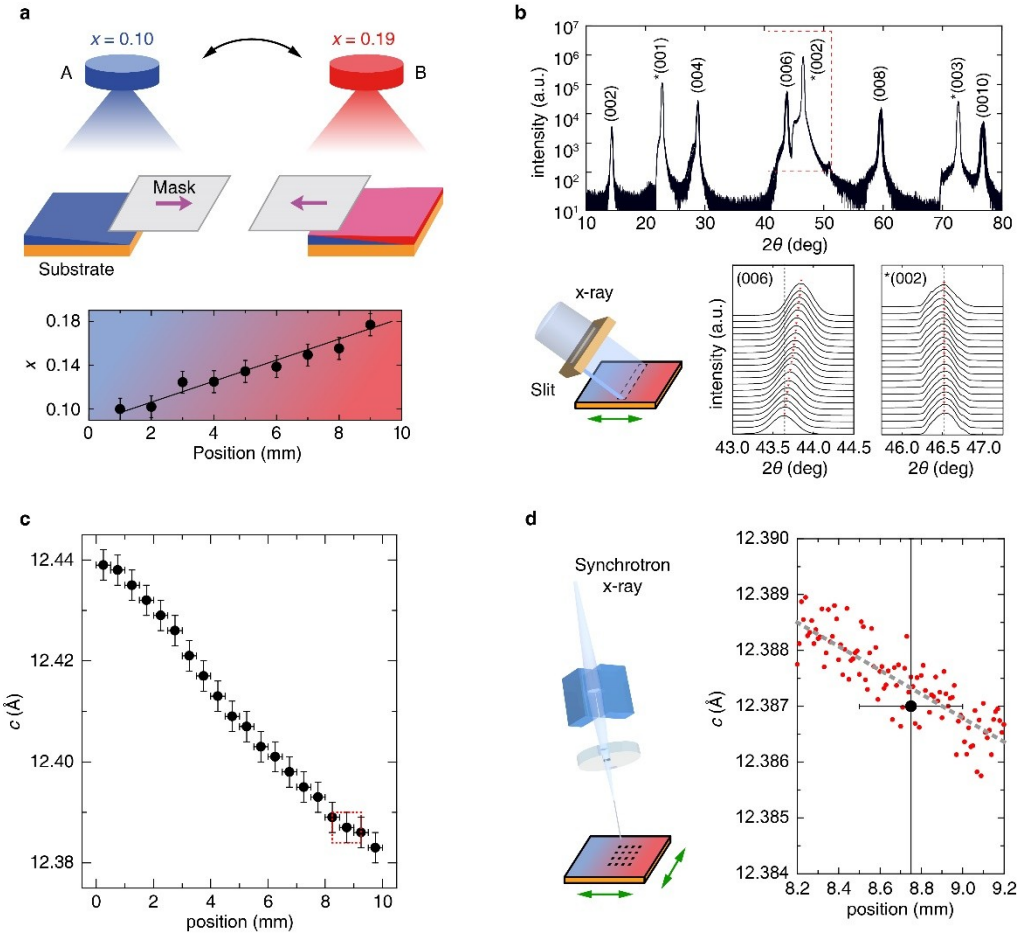

Figure 1 | Combinatorial synthesis and structural characterization at multi-scale. **a,** Upper: Schematic illustration of the continuous-composition-spread combinatorial epitaxial growth on a $SrTiO_3$ (STO) single crystal substrate. Once a target A is ablated by laser pulses, a metal mask moves along the substrate in half a period time and results in a linear distribution of component A. In the other half period, the other target B is ablated for a reverse distribution by moving the mask in the opposite direction. A desired thickness of the combinatorial film can be achieved by setting corresponding periods of deposition. Lower: the position dependence of the Ce doping level mapped by a microprobe wavelength dispersive spectroscopy (WDS). **b,** Upper: The $\theta/2\theta$ x-ray diffraction (XRD) spectra obtained by the regional structural characterization at mm scale with the x-ray beam scans along the film through a narrow slit, scanning from one end (x = 0.10) to the other end (x = 0.19) of the STO substrate. The peaks labeled with "*" are from the STO substrate. Lower: The schematic illustration of the measurement configuration and the magnified image of the dashed line box region in the upper panel, corresponding to the LCCO (006) and STO (002) peaks, respectively. The lines are vertically shifted for clarity. The red reverse triangles label each peak position and the vertical dashed line is an aid for naked eyes to distinguish the magnitude of the peak shift. **c**, The position dependence of the calculated c-axis lattice constant. **d**, left: The schematics of the micro-region structural characterization at μm scale. Right: The position dependence of the c-axis lattice constant by the micro-region (red) and large scale (black) characterizations, corresponding to the region depicted by the red box in panel **c**.

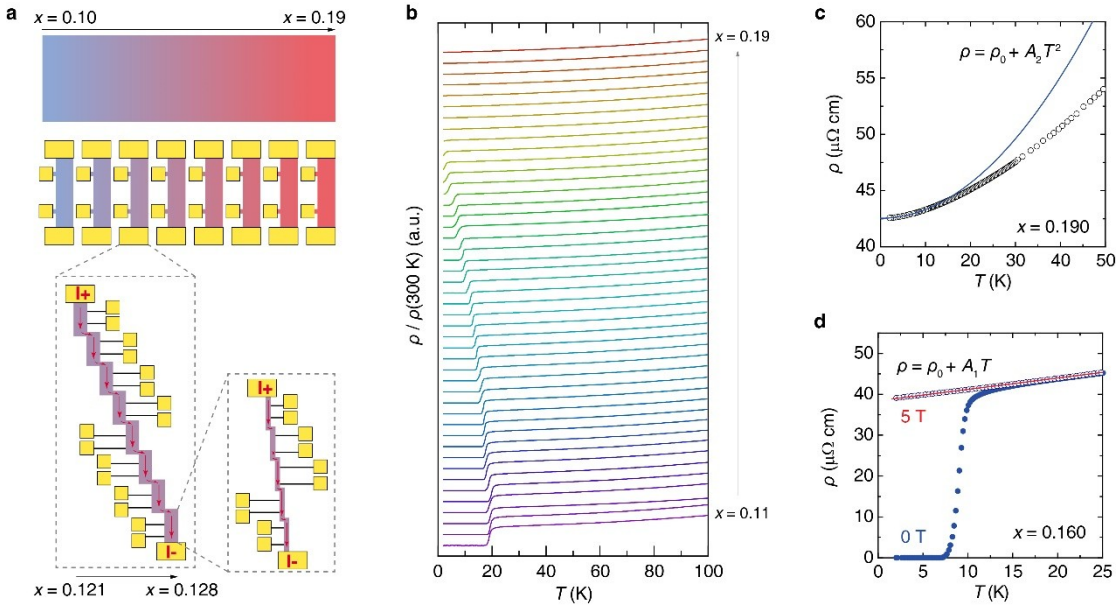

Figure 2 | Micro-region characterizations of electrical transport properties. a, Configuration of the micro-bridges for transport measurements patterned by standard photo-lithography. There are three types of pattern array with different microbridge widths: 0.9, 0.1 and 0.02 mm from the widest to the narrowest. In this way, the spatial resolution of the transport measurement can reach the scale of 20 μm, comparable to the micro-region structural characterization. **b,** Temperature dependence of the resistivity (ρ-T) for different bridges. The resistivity is normalized by the value at 300 K and the curves are vertically shifted for comparison. From the bottom to top, the doping varies from x = 0.10 to x = 0.19. The inverted red triangles roughly label the onset of the superconducting transition. **c,** Temperature dependence of the resistivity for the doping at the right side of the superconducting dome, x = 0.190. The solid line is the fitting using the Fermi liquid formula: $\rho = \rho_0 + A_2T^2$. **d,** Temperature dependence of the resistivity for a superconducting bridge with T_c ~ 10 K (filled circles) (x = 0.160), with a magnetic field of B = 5 T (empty circles) applied perpendicular to the film. The red straight line is the linear fitting $\rho = \rho_0 + A_1T$.

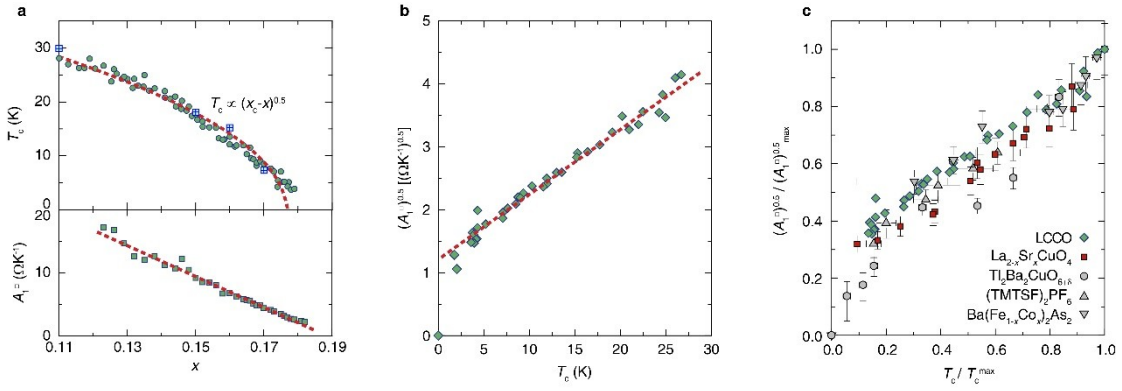

Figure 3 | Quantitative law revealed by the sets of systematic data. a, Doping dependence of T_c (top) and $A_1^{\square}$ (bottom). Across the full film doping range, T_c exhibit a square root dependence on doping: $T_c \propto (x_c\text{-}x)^{0.5}$, while $A_1^{\square}$ shows an explicit linear dependence on doping (red dashed line in the bottom panel). The blue squares in the top panel are extracted from Ref. [9]. **b,** $(A_1^{\square})^{0.5}$ as a function of T_c extracted from the *R-T* curves. The red dashed line shows the linear fitting. **c,** The correlation between $(A_1^{\square})^{0.5}$ and T_c for different systems from literature, with $(A_1^{\square})^{0.5}$ and T_c normalized by their respective maximal values. LSCO extracted from Ref. [20], $(TMTSF)_2PF_6$, $Tl_2Ba_2CuO_{6+\delta}$ and $Ba(Fe_{1-x}Co_x)_2As_2$, from Ref. [10] and references therein, respectively.